

Generation of Uncertainty-Aware High-Level Spatial Concepts in Factorized 3D Scene Graphs via Graph Neural Networks

Jose Andres Millan-Romera¹, Muhammad Shaheer^{1,†}, Miguel Fernandez-Cortizas^{1,†},
Martin R. Oswald², Holger Voos¹, and Jose Luis Sanchez-Lopez¹

Abstract— Enabling robots to autonomously discover high-level spatial concepts (e.g., rooms and walls) from primitive geometric observations (e.g., planar surfaces) within 3D Scene Graphs is essential for robust indoor navigation and mapping. These graphs provide a hierarchical metric-semantic representation in which such concepts are organized. To further enhance graph-SLAM performance, Factorized 3D Scene Graphs incorporate these concepts as optimization factors that constrain relative geometry and enforce global consistency. However, both stages of this process remain largely manual: concepts are typically derived using hand-crafted, concept-specific heuristics, while factors and their covariances are likewise manually designed. This reliance on manual specification limits generalization across diverse environments and scalability to new concept classes.

This paper presents a novel learning-based method that infers spatial concepts online from observed vertical planes and introduces them as optimizable factors within a SLAM backend, eliminating the need to handcraft concept generation, factor design, and covariance specification. We evaluate our approach in simulated environments with complex layouts, improving room detection by 20.7% and trajectory estimation by 19.2%, and further validate it on real construction sites, where room detection improves by 5.3% and map matching accuracy by 3.8%. Results confirm that learned factors can improve their handcrafted counterparts in SLAM systems and serve as a foundation for extending this approach to new spatial concepts.

I. INTRODUCTION

High-level spatial concepts (e.g., rooms and walls) inferred from observable geometric primitives (e.g., vertical planes) enable robots to construct a richer and more human-interpretable understanding of their environment through 3D Scene Graphs (3DSGs) [1]. This widely adopted representation encodes metric-semantic entities as nodes and their relationships as edges within a hierarchical graph, yet it does not capture the probabilistic dependencies among these entities. Factorized 3DSG [2] addresses this limitation by explicitly modeling high-level semantic entities as optimization factors within the

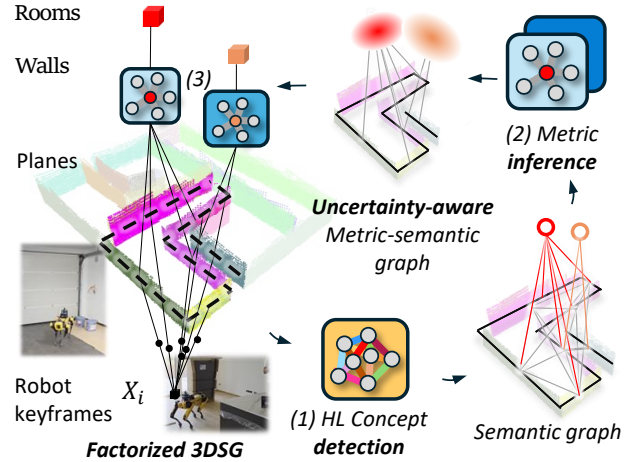


Fig. 1: **System Overview.** An initial graph by proximity is set from the *plane* nodes inside a F3DSG. Upon a GAT-based edge classification, planes are clustered, generating a *room* or *wall* high-level node per cluster. They receive a geometric definition from a different GNN and are incorporated into the F3DSG along with the factors and their covariances.

pose graph. Unlike approaches where such concepts exist only as post-processed scene descriptors [3], this formulation enables hierarchical dependencies (from low-level keyframes through geometric primitives to high-level concepts) to jointly refine both the robot trajectory and the scene representation, allowing semantic understanding to directly improve SLAM performance, which in turn enhances downstream tasks such as global localization [4], and path planning [5].

However, current methods for high-level spatial concept generation typically rely on concept-specific handcrafted algorithms that operate under restrictive assumptions. For example, [3] uses a room detection based on free space clustering, while [6] detects *rooms* using a heuristic histogram over object features. Although these methods construct 3DSGs with multiple semantic layers, they do not model high-level entities as optimization factors in the pose graph.

In [2], the factorization of these high-level concepts was introduced, demonstrating their capability to improve the SLAM performance through joint optimization. In this direction, [7], aim to generalize the concept detection method by learning pairwise relations among *planes* with two models, one for *walls* and one for rectangular *rooms*. Nevertheless, in these methods, geometric factor definitions and their covariance remain handcrafted per concept and tied to the number of observed primitives, which ultimately hinders generalization

¹Authors are with the Automation and Robotics Research Group, Interdisciplinary Centre for Security, Reliability and Trust (SnT), University of Luxembourg. Holger Voos is also associated with the Faculty of Science, Technology and Medicine, University of Luxembourg, Luxembourg. {jose.millan, muhammad.shaheer, miguel.fernandez, holger.voos, joseluis.sanchezlopez}@uni.lu

²Author is with the University of Amsterdam. m.r.oswald@uva.nl
† These authors contributed equally.

* This work was partially funded by the Fonds National de la Recherche of Luxembourg (FNR) under the projects 17097684/RoboSAUR and C22/IS/17387634/DEUS.

* For the purpose of Open Access, and in fulfillment of the obligations arising from the grant agreement, the authors have applied a Creative Commons Attribution 4.0 International (CC BY 4.0) license to any Author Accepted Manuscript version arising from this submission.

to new high-level spatial concepts.

This paper presents a novel learning-based method to generate online high-level spatial concepts of a Factorized 3DSG (F3DSG) as optimizable factors that are integrated into a SLAM backend. The presented work demonstrates this approach on rooms and walls conditioned on observed vertical planes, reducing the need to handcraft both the generation of these concepts along with their factor and covariance definition. Our learning-based framework **(i)** detects the semantic-only 3DSG of these high-level spatial concepts with a per-concept confidence level, based on learned pairwise relations and temporal stabilization, **(ii)** learns to predict metric node attributes as centroids and their uncertainty for all generated nodes in the 3DSG, and **(iii)** defines learned factors with covariances computed from the semantic confidence and geometric prediction uncertainty, completing the F3DSG to be integrated in factor-graph SLAM.

We validate our method in a variety of indoor man-made environments, integrating them into state-of-the-art F3DSG-based SLAM frameworks.

II. RELATED WORK

A. Generation of high-level spatial concepts in 3DSGs

The generation of 3DSGs has progressed from merely placing observed objects and linking them by spatial proximity to modeling their semantic and geometric *pairwise* relations [8], and extended to open-world [9]. They have excelled in applications like planning [10] or reasoning about functional relationships [11]. However, these remain pairwise properties that can be resolved from the two connected nodes alone. More recent works go beyond pairwise relations to capture higher-order, set-level relations, such as belonging to the same room, which can only be determined by considering how multiple surrounding nodes are arranged together. A prominent example is the notion of *rooms* or *spaces*, whose layouts were first inferred from 2D occupancy maps [12]. This concept was subsequently integrated into 3DSGs by generating new high-level nodes and edges connecting to related low-level nodes via 3D free-space clustering [2], [3], traversability [13] or similar concept-specific geometric methods for outdoor environments [14]. These methods are largely ad hoc: they can excel at detecting specific set-level properties, but do not readily generalize to others. To overcome this limitation, other works classify observed objects into high-level nodes based on free-space, semantics, and relations between them. [15] employs a learned ontology to group objects into higher-level nodes, while Clio [16] employs CLIP embeddings for task-tailored clustering. However, they do not generalize to structural elements of indoor environments, such as walls, and they are limited to semantic classification, not providing a metric definition of the created node.

On its side, graph completion aims to infer the unobserved part of a partially observed graph, including *missing nodes* and their incident edges as a conditional reconstruction problem [17]. Deep, structure-conditioned generators explicitly *grow* the graph by autoregressively adding new nodes and connections on top of a given conditioning subgraph [18].

While most prior work targets synthetic graphs and molecules, robotics is increasingly adopting learning-based graph completion techniques for 3DSGs. For instance, [7] detects new *wall* and *room* nodes by classifying semantic relations among plane primitives, thereby extending the scene graph beyond observed elements; yet it employs a separate Graph Attention Network (GAT) [19] per concept type, assumes rectangular layouts, and does not predict centroids for newly generated nodes.

Beyond detecting only graph topology, Graph Neural Networks (GNNs) [20] can directly regress continuous node attributes conditioned on structure and attributes of other nodes, enabling differentiable pipelines [21]. Adversarial generators align synthetic node attributes with structure [22]; disentangled frameworks separate attribute factors for controllability [23]; and constraint-driven generators impose explicit validity to ensure consistency among attributes and edge structure, as in constrained VAEs for molecule design [24]. However, these conditional methodologies have not been applied to the continuous attributes of high-level spatial concepts in 3DSGs.

B. Learnable, Uncertainty-Aware Factor Graphs

Factor graphs are the standard abstraction for large-scale probabilistic inference in SLAM, allowing heterogeneous constraints to fuse through sparse nonlinear least squares optimization [25]. Recent work couples scene graph structure to estimation, either by adding semantic priors to constrained factor graphs or by importing scene graph cues into the optimizer state [26]. *S-Graphs+* [2], [7] integrates a hierarchical 3DSG directly into the optimization state and improves trajectory and map accuracy, but defines each semantic concept (room–plane, etc.) with manually designed factors and fixed covariances, limiting extensibility. In parallel, graph learning has begun to predict continuous factors with GNNs [21], and fully Bayesian graph convolutional networks estimate epistemic variance via Monte-Carlo dropout [27]. Several SLAM systems already modulate information matrices with external semantic-confidence scores, as in Probabilistic Data-Association SLAM [28] and Dynamic Covariance Scaling (DCS) [29]. Exploring data-driven factors in graphs, [30] demonstrates its use in anchor-based positioning via Bayesian inference. However, these techniques have not been applied to robotic F3DSGs, as current systems lack a unified and generalizable approach that learns and integrates geometric factors with uncertainty estimates capturing both semantic relation confidence and geometric prediction uncertainty for newly instantiated high-level nodes.

III. METHODOLOGY

A. Introduction

Background. The SLAM backend incrementally constructs a factor graph composed of a *keyframe layer* and a *plane layer*. The *keyframe layer* captures the robot trajectory, with consecutive keyframes connected through odometry factors. The *plane layer* maintains persistent vertical planar landmarks extracted from LiDAR, where each plane π is parameterized by its centroid, unit normal vector, and spatial extent. To

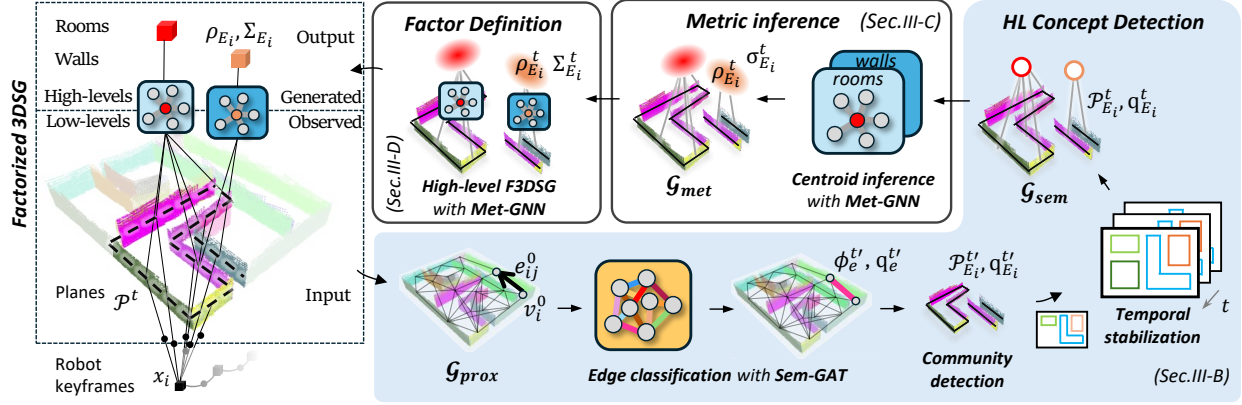


Fig. 2: **System architecture.** After reception of the *plane* layer from the F3DSG of the SLAM backend, every node is connected with its K neighbours, building the initial graph by proximity. It is fed to the Sem-GAT, which classifies the edges into *same room* or *same wall*. Those are separately clustered, leveraging cycles for *same room* ones, and generating a *room* or *wall* semantic nodes for each cluster if it is consistent with previous observations. Afterwards, the geometric origin of the new nodes is inferred by its Met-GNN depending on the concept. A new factor, along with its covariance, is defined for every new node and incorporated into the F3DSG for its use by the SLAM backend.

improve robustness, noisy detections are rejected and overlapping planes are merged. The resulting plane observations $\mathcal{P} = \{\pi_0, \dots, \pi_n\}$ constitute the input to our method.

System overview. Each time the *plane* layer of SLAM backend is updated, our method infers a high-level graph and its connecting factors in three stages: (1) semantic detection groups planes into higher-level concepts such as rooms and walls using a GAT-based architecture, (2) metric definition uses a GNN to predict centroids for the resulting high-level nodes, and (3) uncertainty-aware factor definition derives geometric constraints and covariances from the learned metric and semantic confidences for integration into the F3DSG. We employ two separate neural architectures to keep the semantic and metric components modular and to reuse the centroid predictor in factor construction. The inferred room and wall nodes are added above the plane layer and connected to their associated planes through factors, completing the F3DSG.

B. High-Level Concept Detection

Initial graph. After each plane set observation \mathcal{P}^t at time t , we build a *directed* proximity graph $\mathcal{G}_{\text{prox}}$ by connecting every plane π to its k nearest neighbors (k-NN) by centroid-centroid Euclidean distance. The features are computed using normalized plane features in a 2D projection space. To maintain translation and rotation invariance, the initial node embedding v_i^0 is limited to its length, while edges encode local relative geometry: the Euclidean distance between centroids d_{ij} , the bearing between them φ_{ij} , and the relative angle between normals α_{ij} . The bearing and the relative angle of the normals are expressed in the local-frame construction, yielding rotation and translation invariant descriptors, but are dependent on the reference frame of the i -th node, which is different to j -th node, imposing the need for a directed graph using a direction for each node.

Edge classification. A GAT (Sem-GAT) provides the probability $p_{ij,\theta}$ of each edge e_{ij} to be classified as ϕ :

$$p_{ij,\theta}(\phi | e_{ij}, \mathcal{G}_{\text{prox}}), \phi \in \{\text{same-room}, \text{same-wall}, \text{none}\} \quad (1)$$

Via message passing, the encoder simultaneously updates node and edge embeddings. Eq. (2) updates node embeddings via GAT layers that are max-pooled and passed to an MLP g_v . Parallely, Eq. (3) updates edge embeddings via an MLP g_e , where v_i^l and e_{ij}^l represent the node and edge embeddings at layer l and $\mathcal{N}(i)$ is the vicinity of node i . In Eq. (4), node and edge embeddings of the last hop are jointly decoded with an MLP g_d that outputs logits c_{ij} , followed by a softmax to obtain class probabilities. Training details in Sec. IV.

$$v_i^{l+1} = g_v\left([v_i^l, \max_{j \in \mathcal{N}(i)} \text{GAT}_H(v_i^l, e_{ij}^l, v_j^l)]\right) \quad (2)$$

$$e_{ij}^{l+1} = g_e\left([v_i^l, e_{ij}^l, v_j^l]\right) \quad (3)$$

$$p_{ij} = \text{softmax}\left(g_d([v_i^L, e_{ij}^L, v_j^L])\right) \quad (4)$$

Let $\phi_{ij} = \arg \max_{\phi} (p_{ij})$ be the predicted class. To compute epistemic uncertainty, we follow the Bayesian approximation of dropout proposed by [31], applying dropout to all linear layers and keeping it active at test time. We then run stochastic forward passes per edge to define the semantic confidence $q_{i,j}^t = \text{Var}_{m=1}^M [\phi_{ij}^{(m)}]$.

To ensure robustness, only edges with $q_{i,j}^t$ over a threshold τ_e are accepted as *same-room* or *same-wall*, otherwise they are set to *none* class. Accounting for the case when both directions $i \rightarrow j$ and $j \rightarrow i$ are present, both are merged into a single edge e , rendering the graph undirected. We set the class of the merged edge, ϕ_e^t as the one with highest confidence, set as q_e^t .

Community detection. To detect the existence of high-level entities (rooms and walls) $E_i = \bigcup_i \{R_i, W_i\}$, we identify communities $\mathcal{P}_{E_i}^t$ as subsets of planes in \mathcal{P}^t , whose internal edges are classified as *same-entity*. In the case of rooms, communities are obtained by forming an undirected subgraph from edges classified as *same-room* weighted by q_e^t . Greedy modularity maximization [32] receives this graph and yields the room communities $\mathcal{P}_{R_i}^t$ with a different weight $q_{R_i}^t$ each. Since walls only contain two planes, one community $\mathcal{P}_{W_i}^t$ is defined for each *same-wall* edge along with its associated $q_{W_i}^t$.

Temporal stabilization. We account for room and wall perception changes that may occur when the geometry of planes is updated or when new planes are observed over the entire *planes* layer. At $t > 0$, current communities \mathcal{P}_C^t are matched to tracked communities $\mathcal{P}_C^{0:t-1}$ by the Community Matching \mathcal{CM} module using intersection-over-union similarity $IoU(\cdot, \cdot) \geq \tau_J$ threshold with a hit/miss policy (initiate new tracks when unmatched; generate after n similar observations; retire after o misses).

$$\mathcal{P}_{E_i}^t = \mathcal{CM}(\mathcal{P}_{E_i}^{0:t-1}, \mathcal{P}_{E_i}^t) \quad (5)$$

To stabilize decisions over time we use an *exponential moving average (EMA)* of intra-communities confidence,

$$q_{E_i}^t = \beta q_{E_i}^{0:t-1} + (1-\beta) q_{E_i}^t \quad (6)$$

where $q_{E_i}^{0:t-1}$ is the confidence of the existing associated set $\mathcal{P}_{E_i}^{0:t-1}$, $q_{E_i}^t$ is the estimated confidence of the newly detected set $\mathcal{P}_{E_i}^t$, and $\beta \in [0, 1)$ controls smoothing. Finally, any set with $q_{E_i}^t$ over a threshold τ_{sn} spawns a *room* or *wall* node, connected to its member planes to form \mathcal{G}_{sem} .

C. Metric Inference

We extend \mathcal{G}_{sem} by predicting the centroids of the high-level nodes, yielding the metric-semantic graph \mathcal{G}_{met} . We define a *Met-GNN* architecture trained separately for each high-level spatial concept type (See Sec. IV).

For each community E_i and its emerged node, we form an induced star graph with its incident *plane* nodes \mathcal{P}_{E_i} . Plane features π_j are the centroid \mathbf{p} , unit normal \mathbf{n} , and length ℓ (normalized features), expressed in the current map frame; no edge features are used. To account for complex centroid definitions in the training dataset, Met-GNN performs a single-hop message passing with MLP $f_{\theta_C}^n$ from planes to the high-level entity, followed by mean pooling (permutation invariance over \mathcal{P}_{E_i}) and another MLP $f_{\theta_C}^e$ that outputs a 2-dimensional centroid, as defined in Eq. (7):

$$\rho_{E_i} = f_{\theta_C}^e(\text{mean}(f_{\theta_C}^n(\mathcal{P}_{E_i}^t))), \quad (7)$$

To quantify epistemic uncertainty at time t , we apply dropout in all linear layers with stochastic forward passes per high-level entity; the sample variance of the predicted centroid yields $\sigma_{E_i}^t$ (per-dimension), which are required for composing factor covariances.

D. Factor Graph Definition

Factor definition. We attach a *single multi-plane factor* to each high-level entity, connecting its centroid variable to its supporting planes: an N -ary factor for a room (all planes in \mathcal{P}_{R_i}) and a binary factor for a wall (its two planes). These factors enforce geometric consistency via the learned predictors from Sec. III-C.

For a node of the community \mathcal{P}_{E_i} with previous centroid variable $\rho_{E_i}^t$ and plane variables $\{\pi_j \in \mathcal{P}_{E_i}\}$, the costs are defined as:

$$\kappa_{E_i} = \rho_{E_i}^t - f_{\theta_R}(\mathcal{P}_{E_i}^t) \quad (8)$$

Each factor contributes to the quadratic cost $\|\kappa\|_{\Sigma}^2$. Jacobians of all learned-factor residuals with respect to centroid and plane variables are computed by automatic differentiation in the optimizer.

Covariance definition. Let $\sigma_{E_i}^t \in \mathbb{R}_{>0}^2$ be the predictive variance from Met-GNN (Sec. III-C) estimated via Monte-Carlo dropout samples for node i . We form the factor covariance Σ_i as a combination of $\sigma_{E_i}^t \in \mathbb{R}^2$ with the tracked community confidence $q_{E_i}^t$ via DCS:

$$\Sigma_{E_i}^t = \alpha \sigma_{E_i}^t / \max(q_{E_i}^t, \varepsilon) \quad (9)$$

with $\alpha, \varepsilon > 0$ chosen on a validation set. This positive semidefinite form down-weights a factor (larger covariance) when geometric uncertainty is high or semantic confidence is low.

Factor integration. We inject planes-to-room and planes-to-wall factors for all inferred high-level spatial concepts into the F3DSG of the SLAM backend, enabling joint optimization of plane, room, and wall geometry together with the keyframes. To maintain consistency with prior observations, we add factors for newly inferred concepts, update those whose supporting planes change (using the revised centroids), and remove factors for concepts no longer observed.

IV. TRAINING

Training datasets. We employ a custom synthetic dataset generator and MSD public dataset [33], both mimicking common building layouts in the form of graphs. They include all the required nodes, edges, and their semantic and geometric definitions of the layers of the SLAM backend, excluding the keyframes. To make the synthetic dataset as realistic as possible, L-shaped *rooms*, *wall* thickness, *wall* length, *plane* dropout, and number of planes in a room can be tuned. Additionally, we post-process the data with noise in orientation and position for all geometric definitions. From these graphs, we extract subgraphs to form inputs and ground truth, enabling unlimited training samples with target features that complement the limited coverage of MSD.

Edge classification. See Fig. 3 left. To train Sem-GNN, we generate a full synthetic layout containing all *planes* along with the *same room* and *same wall* edges. The graph is used as ground truth for training, where we define the initial graph by proximity by connecting each node to its $k = 15$ nearest neighbors. The optimization process is guided by the cross-entropy criterion, using the Adam optimizer. Hyperparameter search selected a 2-hop message-passing backbone with 8 attention heads. The decoder g_d uses hidden widths [188, 236], while the encoder MLPs g_v and g_e use 18 and 55 hidden channels, respectively. Training uses a learning rate of 1.56×10^{-3} with batch size 128. Monte Carlo dropout is set to 10 passes.

Origin inference. See Fig. 3 right. Layouts of the MSD dataset are used to train the Met-GNNs by extracting subgraphs for each higher-level node (*room* or *wall*). In this dataset, the method to define the center is unknown. The high-level node, its adjacent *plane* nodes, and the edges between them are used as input to the Met-GNN, with the ground

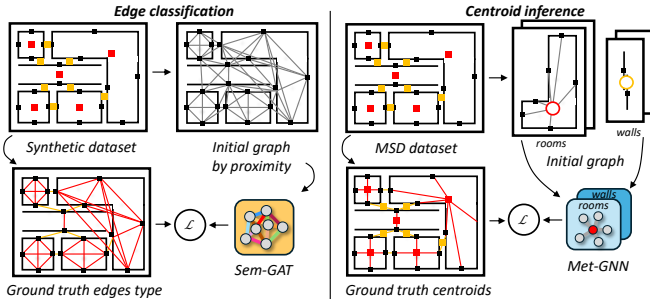


Fig. 3: **Training processes.** For both architectures, from the training dataset the initial graph is extracted and provided as input to the network, whose output is compared to the ground truth to compute the loss

Method	Semantic detection			Factors		
	Room	Wall	SU	SU	MU	Definition
Hydra [3]	Free Space	×	×	×	×	×
S-Graphs [2]	Free Space	×	×	×	×	Classic
SghsGnn [7]	GNN ¹	GNN ¹	×	×	×	Classic
Ours-NF	GNN ²	GNN ²	✓	×	×	Classic ³
Ours-SF	GNN ²	GNN ²	✓	✓	×	GNN ⁴
Ours	GNN ²	GNN ²	✓	✓	✓	GNN ⁴

TABLE I: Baseline and ablation comparison relative to the high-levels of the 3DSG and the factor graph. SU/MU: semantic/metric uncertainty, 1: Separate architectures, 2: joint architecture, 3: average of centroids, 4: learned architecture.

truth origin for the high-level node removed. The optimization process is guided by the mean squared error (MSE) criterion, and the Adam optimizer is used. Hyperparameter search for θ_C selected a single hidden layer of size 23 for $f_{\theta_C}^e$ and two hidden layers of sizes 20 and 15 for $f_{\theta_C}^n$. Training uses a learning rate of 3.50×10^{-5} with batch size 64. Monte Carlo dropout is set to 10 passes.

V. EVALUATION

A. Evaluation methodology

Baselines. As summarized in Tab. I, we compare the 3DSG generation against three baselines: free-space room detection in *Hydra* [3], free-space room detection in *S-Graphs* [2], and learning-based wall and room detection in *SghsGnn* [7].

SLAM performance is compared to *S-Graphs* and *SgrhsGnn*, while *Hydra* is omitted as its high-level nodes do not define factors for SLAM optimization. We provide two ablations to our full method (*Ours*). First, we only use semantic information to compute the covariance, setting $\sigma_{E_i}^t = \mathbf{1}_{\mathbb{R}^2}$ (*Ours-SF*). Second, we substitute Met-GNN for a naive factor that averages centroids with the handcrafted factor and sets almost-zero covariance (*Ours-NF*). To ensure comparability, all the methods use *S-Graphs+* [2] as the SLAM backend. This backend had already demonstrated improvements over state-of-the-art LiDAR SLAM systems without high-level factors (e.g., FAST-LIO2 [34]) in terms of trajectory error and map accuracy. Our evaluation thus isolates the contribution of different high-level concept generation methods within this shared backend.

Evaluation environments. Since public datasets do not capture the layout complexity and the ground truth of high-level concepts, point clouds, and trajectories required to evaluate our high-level concept detection and factor-graph SLAM, we have recorded 8 environments simulated in Gazebo with data acquired with a 3D LiDAR sensor (denoted as S-) and 5 real-world environments R- recorded with a 3D LiDAR in a Boston Dynamics Spot[®] in offices and houses in construction with visible walls, as exemplified in Fig. 1. As shown in Fig. 4, S- covers edge cases with many non-rectangular and large rooms while R- includes real environments with at least one non-rectangular room, challenging the capabilities of existing baselines.

High-level 3DSG detection metrics. We define a metric to evaluate the quality of the set of planes associated with each high-level spatial concept, quantifying both correct coverage and error rate, given their impact on the structural accuracy of the graph and subsequent SLAM performance. As the concepts evolve during exploration, the final snapshot is used once the entire environment has been explored.

Let $\mathcal{R} = r_j$ be the set of ground-truth entities (exemplified in room for clarity) and $\hat{\mathcal{R}} = \hat{r}_i$ the set of predicted entities of the same type. Each entity is represented by the set of planes it is connected to, denoted $\mathcal{P}(r_j)$ and $\mathcal{P}(\hat{r}_i)$, respectively. The ground-truth associations between planes and entities are defined from a reference map of each scene. For each method, the predicted associations are visually verified against this ground truth. In the case of *Hydra*, since it does not provide any plane-room association, each plane is visually associated with the closest free-space cluster within a range. Each predicted entity is then paired with the ground-truth entity that shares the most planes, forming a one-to-one assignment.

With the confusion matrix defined in Eq. (10), precision, recall, and intersection over union (IoU) are similarly computed for rooms and wall entities.

$$\begin{aligned}
 TP &= \mathcal{P}(\hat{r}) \cap \mathcal{P}(r), \\
 FP &= \mathcal{P}(\hat{r}) \setminus \mathcal{P}(r), \quad FN = \mathcal{P}(r) \setminus \mathcal{P}(\hat{r})
 \end{aligned} \tag{10}$$

SLAM performance metrics. We assess Average Trajectory Error (ATE) in S- as the ground truth trajectory is not available in R-. We compute Map Matching Accuracy (MMA) in S- and R- as RMSE between ground truth and estimated point clouds with visually aligned origins for R-, where ground truth origin alignment is not available. We assess as well the required runtime and the number of variability of generated high-level nodes over the number of plane nodes in $\mathcal{G}_{\text{prox}}$.

Hardware. All experiments were conducted on a laptop equipped with an Intel[®] Core[™] i9-12900H processor (14 cores, 20 threads, base frequency 2.9 GHz, turbo up to 5.0 GHz), and an NVIDIA T600 Laptop GPU with 4 GB VRAM (driver 535.183.01, CUDA 12.2).

B. Results and Discussion

High-level 3DSG detection results. Tab. II shows consistent improvements in room detection across both simulation and real datasets: 3.4%, 18.2%, and 20.7% (precision/recall/IoU)

Method	Simulation								Real					
	S1	S2	S3	S4	S5	S6	S7	Avg	R1	R2	R3	R4	R5	Avg
Precision														
Hydra	68.4	66.7	51.6	78.9	88.9	100	95.8	78.8	60.0	70.8	38.6	65.0	100	66.9
S-Graphs	62.5	85.7	83.3	81.2	88.9	45.0	68.8	74.4	75.0	86.1	81.8	30.0	41.7	62.9
SghsGnn	85.7	66.7	50.0	80.0	77.8	100	25.0	68.5	75.0	75.0	66.7	50.0	33.3	60.0
Ours	85.7	80.5	66.7	60.0	100	90.0	100	82.2	100	64.3	66.7	60.3	96.0	77.4
Recall														
Hydra	56.2	66.7	43.8	42.6	59.3	77.8	57.3	58.3	36.0	75.0	45.5	66.7	83.3	61.3
S-Graphs	53.0	77.1	66.7	53.1	59.3	33.3	75.0	56.1	42.1	48.8	54.5	20.0	27.8	38.7
SghsGnn	77.1	53.3	38.9	51.7	33.3	66.7	16.7	47.7	42.1	57.1	55.6	46.2	22.2	44.7
Ours	69.6	78.8	66.7	60.0	85.7	90.0	90.0	76.5	79.4	60.2	47.9	54.4	91.0	66.6
IoU														
Hydra	49.6	66.7	32.9	37.2	59.3	77.8	56.7	55.4	36.0	70.8	38.6	65.0	83.3	58.8
S-Graphs	48.8	77.1	66.7	52.1	59.3	29.0	68.8	54.1	42.1	47.1	54.5	20.0	27.4	38.2
SghsGnn	77.1	53.3	38.9	51.7	33.3	66.7	16.7	47.5	42.1	57.1	55.6	44.4	22.2	44.3
Ours	69.6	75.6	66.7	60.0	85.7	90.0	90.0	76.1	79.4	57.8	47.9	50.5	88.3	64.8

TABLE II: Plane-level Precision/Recall/IoU (%) for rooms across methods and LiDAR S- and R- datasets. Best results are highlighted by **first**, **second**, and **third**.

in S- and 9.5%, 4.0%, and 5.3% on real data. Fig. 4 illustrates these improvements with representative layout examples and their detected entities. The performance improvements are particularly notable in edge cases with complex, non-rectangular rooms, showing IoU gains of 44.5% in S5, 30.8% in S7, and 88.7% in R1. Fig. 5 shows how this advantage is distributed across room complexity, particularly in rooms with 3 or 5+ *planes* while maintaining state-of-the-art performance in rooms with 4 *planes*. In particular, L6 features only triangular rooms; S2, S3, S5, and all R- contain six-plane rooms; R4 contains an eight-plane room; and S7 includes non-Manhattan layouts. Since *S-Graphs* and *SghsGnn* target simpler 2 or 4 plane configurations, they maintain the precision but decrease the recall, detecting correctly only a subset of actual planes. *Hydra* maintains comparable recall and IoU for larger rooms but fails on highly complex cases (8 planes or larger areas) in those challenging datasets. Our GAT-based approach successfully detects intricate room geometries that challenge rule-based methods, even though the training set only contains 2, 4, and 6-plane rooms, thanks to the out-of-distribution detection grounded on pair-wise relations and their clustering.

Regarding walls, since they are composed of two planes and both methods detect them either fully correctly or miss them entirely, the three metrics yield similar values; we therefore present only IoU in Tab. III. Ours presents 3.0% higher IoU in S-, while the dedicated GNN of *SghsGnn* performs 1.8% higher in R-, indicating that no method presents statistically significant improvements, and Ours matches the performance of state-of-the-art.

Fig. 6 (Top) presents how the number of instantiated concepts increases monotonically while the variability of its associated plane communities is largely reduced by the *Temporal stabilization* module, which enforces successive consistent detections before a concept is confirmed or updated.

Additionally, we explore the applicability of our framework to different sensory inputs and SLAM backends by integrating

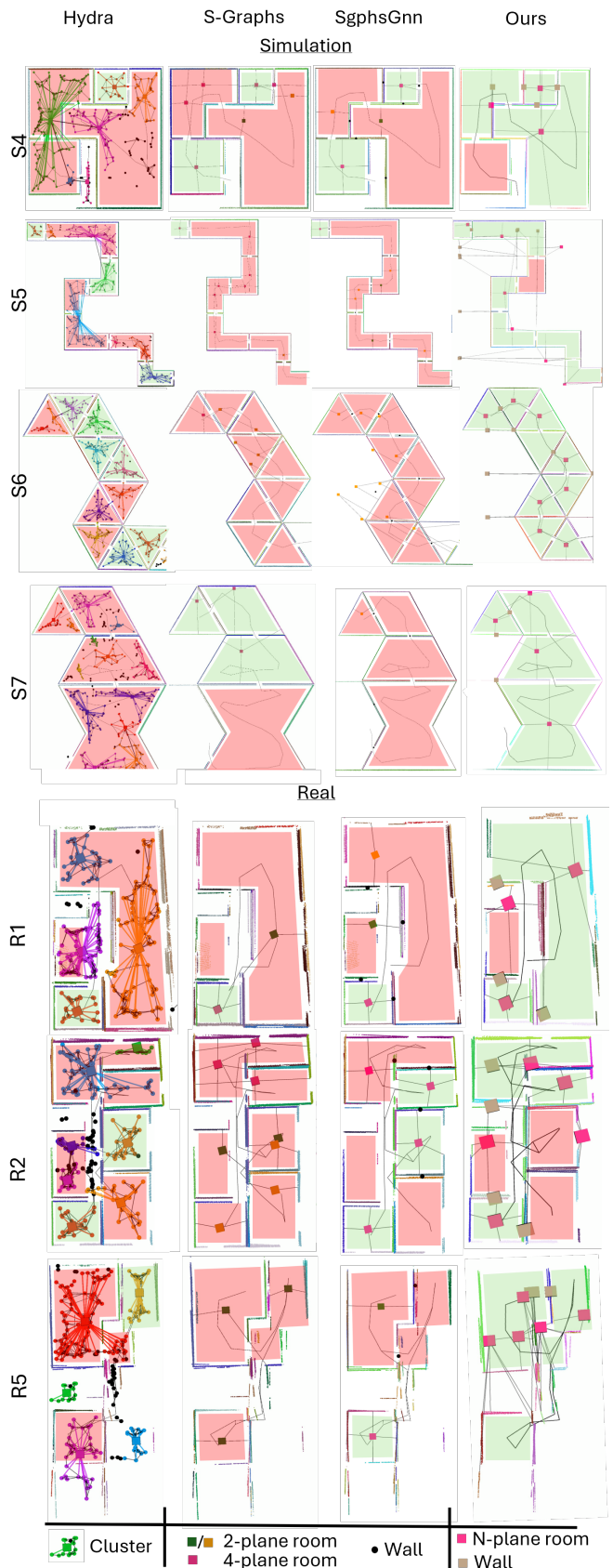


Fig. 4: **3DSG detection from LiDAR data.** Top-down views of RViz representation of the inferred 3DSGs. Rooms *completely detected* (IoU=1) are depicted in GREEN while rooms with at least a wrong plane selection are depicted RED.

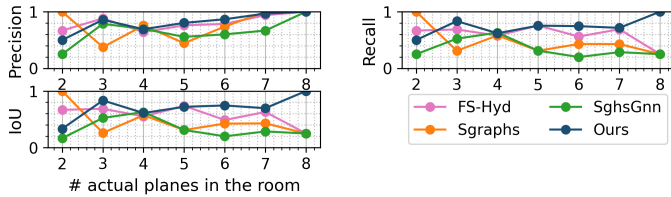


Fig. 5: **3DSG detection over room complexity.** Precision, recall, and intersection over union (IoU) performance of every detection method by number of planes.

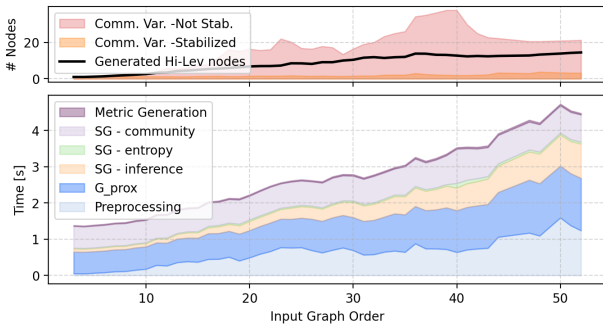


Fig. 6: **Computation times and inference variability.** (Top) Variability of community variables before and after stabilization, and number of generated high-level nodes. (Bottom) Per-stage computation time.

it with visual S-Graphs [35] on 3 real-world RGB-D environments captured with a handheld Intel RealSense D435. As shown in Fig. 7, despite the different data distribution of the sensor, our method correctly detects most rooms and walls, indicating robustness to varying inputs and backend configurations.

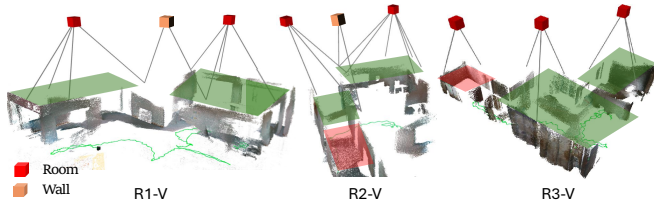


Fig. 7: **3DSG detection from RGB-D data.** Views of the high-level room and wall nodes inferred from the point clouds of the planes. Rooms *completely detected* (IoU=1) are depicted in GREEN while rooms with at least a wrong plane selection are depicted RED.

SLAM performance results.

As shown in Tab. IV, our full method reduces ATE by 19.2% on average in S-, with the largest improvements of 53.8% in S5 and 36.8% in S7, while maintaining performance on the remaining datasets. Note that S5 (non-rectangular) and S7 (non-Manhattan) are large-scale scenarios, where Ours improves room-IoU by +44% and +31%, respectively. This improvement stems from the unique exploitation of room-plane-wall-planes-rooms chains throughout the trajectory, which propagates geometric consistency and reduces drift in scenarios where

Method	Simulation							Real						
	S1	S2	S3	S4	S5	S6	S7	Avg	R1	R2	R3	R4	R5	Avg
SghsGnn	100	66.7	85.7	85.7	100	70.0	66.7	80.0	100	71.4	75.0	86.7	66.7	80.0
Ours	100	75.0	71.4	71.4	85.7	77.8	100	83.0	75.0	66.7	90.9	91.7	66.7	78.2

TABLE III: Plane-level IoU (%) for walls across methods and datasets. Best results are highlighted by **first** and **second**.

Method	S1	S3	S4	S5	S6	S7	S8	Overall
S-Graphs	2.02	3.05	3.40	9.56	3.23	4.83	1.70	3.97
SghsGnn	2.00	2.64	3.05	9.58	3.33	4.27	1.78	3.81
Ours	2.76	2.73	3.14	4.42	3.39	3.54	1.56	3.08
Ours-NF	2.19	2.20	3.09	3.33	2.47	3.27	1.26	2.55
Ours-SF	2.82	2.87	3.25	3.74	3.52	4.33	1.52	3.15

TABLE IV: **Average Trajectory Error (ATE)** [$m \times 10^{-2}$], of S-Graph+ with different detection modules on simulated environments from LiDAR. **Best**, **second**, and **third**

loop closure cannot be applied. Without the metric covariance (*Ours-SF*), the improvement drops to 17.3%, demonstrating the necessity to disable the factor when the uncertainty of the estimation is high. The handcrafted geometric factors (*Ours-NF*) achieve the largest improvement at 33%, as their near-zero covariance suits the low-noise simulated setting.

Regarding the MMA performance presented in Tab. V, the behaviour in S- is similar to ATE, notably improving for 46.5% in L5 and 9% in L7, and maintaining the performance in the rest, presenting a similar behavior to ATE in these environments. The best average improvement is provided by the hand-coded, non-generalizable factors by 12.3% (*Ours-CF*). Our full learning-based factor provides an improvement of 11.0% reduced to 10.8% when not incorporating metric uncertainty into the covariance estimation (*Ours-SF*). When exposed to the real world in R-, our full method presents the largest improvement by 3.8%, while the ablation of the metric uncertainty estimation reduces the improvement to 3.6%, and the naive factor (*Ours-NF*) achieves a comparable improvement, as its near-zero covariance advantage narrows under noisier real-world conditions. Conversely, the learned covariance is more conservative in simulation but better calibrated to real conditions, matching handcrafted performance without per-concept engineering. These results demonstrate that learned inference with learned factors and covariance maintains SLAM performance while providing substantial improvements in edge cases with complex layouts.

Computation time. Fig. 6 (Bottom) indicates that the joint semantic and metric inference times increase monotonically with the number of plane nodes but remain within a few seconds even for the largest graphs, thereby sustaining online operation in parallel with the SLAM back end. More specifically, we observe that the preprocessing of the planes and the semantic inference monotonically increase with order. On its side, the computation of $\mathcal{G}_{\text{prox}}$ and community detection, although considerable initially, are only slightly affected by the order as well. Finally, Entropy computations and metric generation remain minimal compared to the rest. The average computation time of a single factor is $691\mu s$ and $2s$ for the

Simulation								
Method	S1	S3	S4	S5	S6	S7	S8	Overall
S-Graphs	26.36	22.77	22.69	39.88	22.11	20.09	33.68	26.80
SghsGnn	26.40	22.86	22.63	41.03	22.15	20.08	33.74	26.98
Ours	26.53	23.02	22.36	21.32	21.90	18.27	33.53	23.85
Ours-NF	26.58	23.19	22.48	19.27	21.70	17.83	33.53	23.51
Ours-SF	26.47	23.13	22.43	20.79	22.70	18.22	33.47	23.89

Real						
Method	R1	R2	R3	R4	R5	Overall
S-Graphs	76.71	67.15	260.54	33.00	184.91	124.46
SghsGnn	77.31	67.45	258.06	34.27	184.79	124.38
Ours	76.02	65.37	235.70	33.68	187.57	119.67
Ours-NF	76.70	68.25	235.87	31.76	187.38	119.99
Ours-SF	75.81	65.85	234.12	36.66	187.40	119.97

TABLE V: Map Matching Accuracy (MMA) [$m \times 10^{-2}$], of S-Graph+ with different detection modules on simulated (S-) and real (R-) data. **Best**, **second**, and **third**

full optimization process in an environment with 40 planes.

VI. CONCLUSION

This paper presents a learning-based method that generates high-level spatial concepts (rooms and walls) from observed vertical planes and instantiates them as optimization factors within F3DSGs. This removes the need to handcraft concept generation, factor definition, and covariance formulation.

Across complex environments, our approach outperforms room detection baselines, particularly in non-rectangular layouts, while matching state-of-the-art wall detection. Our method yields the strongest SLAM gains in edge cases, though improvements decrease in real environments where predominantly rectangular layouts limit the advantage. In simulation, the handcrafted factor achieves the best ATE, yet both methods converge to equivalent performance in real data, suggesting that refining the learned architecture or training data could close this gap.

Beyond the analyzed performance, the learning-based components are not inherently tied to rooms and walls conditioned on vertical planes. Extending to new high-level spatial concept types requires retraining with appropriate datasets and adapting community detection, but not redesigning factor or covariance formulations, unlike handcrafted approaches, where each concept demands a dedicated geometric design.

REFERENCES

- I. Armeni, Z.-Y. He, J. Gwak, A. R. Zamir, M. Fischer, J. Malik, and S. Savarese, "3D Scene Graph: A structure for unified semantics, 3D space, and camera," in *Proceedings of the IEEE/CVF International Conference on Computer Vision*, 2019, pp. 5664–5673.
- H. Bavle, J. L. Sanchez-Lopez, M. Shaheer, J. Civera, and H. Voos, "S-graphs+: Real-time localization and mapping leveraging hierarchical representations," *IEEE Robotics and Automation Letters*, 2023.
- N. Hughes, Y. Chang, and L. Carlone, "Hydra: A real-time spatial perception system for 3d scene graph construction and optimization," in *Robotics: Science and Systems*, 2022.
- M. Shaheer, J. A. Millan-Romera, H. Bavle, M. Giberna, J. L. Sanchez-Lopez, J. Civera, and H. Voos, "Tightly coupled slam with imprecise architectural plans," *IEEE Robotics and Automation Letters*, vol. 10, no. 8, pp. 8019–8026, 2025.

- S. Ejaz, M. Giberna, M. Shaheer, J. A. Millan-Romera, A. Tourani, P. Kremer, H. Voos, and J. L. Sanchez-Lopez, "Situationally-aware path planning exploiting 3d scene graphs," *arXiv preprint arXiv:2508.06283*, 2025.
- A. Werby, C. Huang, M. BÜchner, A. Valada, and W. Burgard, "Hierarchical open-vocabulary 3d scene graphs for language-grounded robot navigation," in *First Workshop on Vision-Language Models for Navigation and Manipulation at ICRA 2024*, 2024.
- J. A. Millan-Romera, H. Bavle, M. Shaheer, M. R. Oswald, H. Voos, and J. L. Sanchez-Lopez, "Learning high-level semantic-relational concepts for slam," in *2024 IEEE/RSJ International Conference on Intelligent Robots and Systems (IROS)*. IEEE, 2024, pp. 9803–9810.
- J. Wald, H. Dharmo, N. Navab, and F. Tombari, "Learning 3d semantic scene graphs from 3d indoor reconstructions," in *Proceedings of the IEEE/CVF Conference on Computer Vision and Pattern Recognition*, 2020, pp. 3961–3970.
- S. Koch, N. Vaskevicius, M. Colosi, P. Hermosilla, and T. Ropinski, "Open3dsg: Open-vocabulary 3d scene graphs from point clouds with queryable objects and open-set relationships," 2024.
- Q. Gu, A. Kuwajerwala, S. Morin, K. M. Jatavallabhula, B. Sen, A. Agarwal, C. Rivera, W. Paul, K. Ellis, R. Chellappa, C. Gan, C. M. de Melo, J. B. Tenenbaum, A. Torralba, F. Shkurti, and L. Paull, "Conceptgraphs: Open-vocabulary 3d scene graphs for perception and planning," 2023.
- C. Zhang, A. Delitzas, F. Wang, R. Zhang, X. Ji, M. Pollefeys, and F. Engelmann, "Open-vocabulary functional 3d scene graphs for real-world indoor spaces," in *Proceedings of the Computer Vision and Pattern Recognition Conference*, 2025, pp. 19401–19413.
- M. Luperto, T. P. Kucner, A. Tassi, M. Magnusson, and F. Amigoni, "Robust structure identification and room segmentation of cluttered indoor environments from occupancy grid maps," *IEEE Robotics and Automation Letters*, vol. 7, no. 3, pp. 7974–7981, 2022.
- J. Kim, M. Oh, and H. Myung, "Tacs-graphs: Traversability-aware consistent scene graphs for ground robot localization and mapping," in *2025 IEEE/RSJ International Conference on Intelligent Robots and Systems (IROS)*. IEEE, 2025, pp. 6008–6015.
- E. Greve, M. BÜchner, N. Vödisch, W. Burgard, and A. Valada, "Collaborative dynamic 3d scene graphs for automated driving," in *2024 IEEE International Conference on Robotics and Automation (ICRA)*. IEEE, 2024, pp. 11118–11124.
- J. Strader, N. Hughes, W. Chen, A. Speranzon, and L. Carlone, "Indoor and outdoor 3d scene graph generation via language-enabled spatial ontologies," *IEEE Robotics and Automation Letters*, vol. 9, no. 6, pp. 4886–4893, 2024.
- D. Maggio, Y. Chang, N. Hughes, M. Trang, D. Griffith, C. Dougherty, E. Cristofalo, L. Schmid, and L. Carlone, "Clio: Real-time task-driven open-set 3d scene graphs," *IEEE Robotics and Automation Letters*, 2024.
- M. Kim and J. Leskovec, "The network completion problem: Inferring missing nodes and edges in networks," in *Proceedings of the 2011 SIAM international conference on data mining*. SIAM, 2011, pp. 47–58.
- F. Faez, N. Hashemi Dijujin, M. Soleymani Baghshah, and H. R. Rabiee, "Scgg: A deep structure-conditioned graph generative model," *Plos one*, vol. 17, no. 11, p. e0277887, 2022.
- P. Veličković, G. Cucurull, A. Casanova, A. Romero, P. Lio, and Y. Bengio, "Graph attention networks," *arXiv preprint arXiv:1710.10903*, 2017.
- F. Scarselli, M. Gori, A. C. Tsoi, M. Hagenbuchner, and G. Monfardini, "The graph neural network model," *IEEE transactions on neural networks*, vol. 20, no. 1, pp. 61–80, 2008.
- Z. Fang, Z. Zhang, G. Song, Y. Zhang, D. Li, J. Hao, and X. Wang, "Invariant factor graph neural networks," in *2022 IEEE International Conference on Data Mining (ICDM)*. IEEE, 2022, pp. 933–938.
- X. Chen, S. Chen, H. Zheng, J. Yao, K. Cui, Y. Zhang, and I. W. Tsang, "Node attribute generation on graphs," *arXiv preprint arXiv:1907.09708*, 2019.
- W. Zhang, L. Zhang, D. Pfoser, and L. Zhao, "Disentangled dynamic graph deep generation. arxiv 2021," *arXiv preprint arXiv:2010.07276*, 2021.
- W. Jin, R. Barzilay, and T. Jaakkola, "Junction tree variational autoencoder for molecular graph generation," in *International conference on machine learning*. PMLR, 2018, pp. 2323–2332.
- F. Dellaert, M. Kaess, et al., "Factor graphs for robot perception," *Foundations and Trends® in Robotics*, vol. 6, no. 1-2, pp. 1–139, 2017.
- M. Haroon Dupty, Y. Dong, S. Leng, G. Fu, Y. L. Goh, W. Lu, and W. S. Lee, "Constrained layout generation with factor graphs," *arXiv e-prints*, pp. arXiv–2404, 2024.

- [27] S. Ryu, Y. Kwon, and W. Y. Kim, "A bayesian graph convolutional network for reliable prediction of molecular properties with uncertainty quantification," *Chemical science*, vol. 10, no. 36, pp. 8438–8446, 2019.
- [28] S. L. Bowman, N. Atanasov, K. Daniilidis, and G. J. Pappas, "Probabilistic data association for semantic slam," in *2017 IEEE international conference on robotics and automation (ICRA)*. IEEE, 2017, pp. 1722–1729.
- [29] P. Agarwal, G. D. Tipaldi, L. Spinello, C. Stachniss, and W. Burgard, "Robust map optimization using dynamic covariance scaling," in *2013 IEEE international conference on robotics and automation*. Ieee, 2013, pp. 62–69.
- [30] A. Moragrega and C. Fernández-Prades, "A data-driven factor graph model for anchor-based positioning," *Sensors*, vol. 23, no. 12, p. 5660, 2023.
- [31] Y. Gal and Z. Ghahramani, "Dropout as a bayesian approximation: Representing model uncertainty in deep learning," in *international conference on machine learning*. PMLR, 2016, pp. 1050–1059.
- [32] A. Clauset, M. E. Newman, and C. Moore, "Finding community structure in very large networks," *Physical Review E—Statistical, Nonlinear, and Soft Matter Physics*, vol. 70, no. 6, p. 066111, 2004.
- [33] C. van Engelenburg, F. Mostafavi, E. Kuhn, Y. Jeon, M. Franzen, M. Standfest, J. van Gemert, and S. Khademi, "Msd: A benchmark dataset for floor plan generation of building complexes," 2024.
- [34] W. Xu, Y. Cai, D. He, J. Lin, and F. Zhang, "Fast-lid2: Fast direct lidar-inertial odometry," *IEEE Transactions on Robotics*, vol. 38, no. 4, pp. 2053–2073, 2022.
- [35] A. Tourani, S. Ejaz, H. Bavle, M. Fernandez-Cortizas, D. Morilla-Cabello, J. L. Sanchez-Lopez, and H. Voos, "vs-graphs: Tightly coupling visual slam and 3d scene graphs exploiting hierarchical scene understanding," *arXiv preprint arXiv:2503.01783*, 2025.